Thermal Stability and Residual Stresses in Additively Manufactured Single and Multi-material Systems

BIKASH KUMAR and BALILA NAGAMANI JAYA

A sequential coupled thermo-mechanical model was developed for laser-based direct energy deposition of single- IN718 and multi-material IN718-Ti6Al4V systems to monitor the thermal stability, solidification characteristics and origin of the residual stresses in each successively deposited layer in real-time. A qualitative agreement was observed between the model and experimental measurements of temperature field and residual stress in the ten layered build system. The substitution of the IN718 substrate with Ti6Al4V alloy caused remarkable temperature rise (~ 220 K) in the preliminary deposited layers due to the high thermal energy accumulation in Ti6Al4V, leading to relatively low solidification velocity (2.02 mm/s) and large melt pool (0.95 mm). The heat sink effect of the substrate was effective up to the deposition of five-layers. The calculated solidification parameters, i.e., temperature gradient, G and solidification velocity, R suggested a columnar structured interface for both systems in the solidification map. The primary arm dendritic spacing (PDAS) ranging from 8.9 to 21.7 μm increased to 10.8 to 24.6 μm on changing the substrate from IN718 (10IN/IN) to Ti6Al4V (10IN/Ti). The overall tensile residual stress reduced from 655 MPa in the 10IN/IN to 621 MPa in the 10IN/Ti due to the lowered thermal gradient. However, an interesting reversal of maximum tensile residual stress, σ_{11} location from the top (tenth layer) to the first layer occurred on changing the substrate from IN718 to Ti6Al4V due to the substantial difference in the coefficient of thermal expansion (ΔCTE ~ 4.3×10^{-6} K^{-1}) at the interface.

https://doi.org/10.1007/s11661-022-06928-3

I. INTRODUCTION

ADDITIVE manufacturing (AM) is introduced as a computer-controlled rapid manufacturing process that has seen a rapid expansion towards being key technology to produce three-dimensional (3D) objects by depositing single or multi-material in a layer-by-layer fashion.[1–3] The metal AM process is a promising technique since it renders the potential to economically fabricate customized parts with intricate geometries as well as minimize waste and enhance sustainability through repair and refurbishment of expensive parts. The multi-material composite system comprised two or more materials, either in the build section and/or substrate section usually benefit from the differing thermo-physical and thermo-mechanical properties of both the materials.[4] The AM approach is capable of fabricating multi-material parts in a single step. Although AM is the keystone of the advancement in contemporary manufacturing industries, there are some drawbacks, for instance, sharp temperature gradient, excessive thermal stress/strain, unavoidable tensile residual stress, and heterogeneous microstructural evolution that limit this technique.[5–7] The development of residual stress is most often cause of build failure in the metal AM process.[8,9] The nature of stress tensile or compressive depends on the magnitude of CTE possessed by build or substrate material in multi-material system.[10] Thus, post-manufacturing heat treatments can be designed if the in-process residual stress distribution is well-known apriori. Hence, qualitative and quantitative estimation of developed residual stresses becomes a pivotal step in the design workflow.

The parts fabricated using dual-phase Ti alloy and Ni-based superalloy are of great importance in several industries such as aerospace, biomedical, nuclear for producing miniature-to-large components including turbine blades, combustion chambers, nuclear reactor, medical devices, stent, bone implant, aeronautic and military components, etc. and have been successfully processed using AM.[11–13] The Ti6Al4V $\alpha + \beta$-alloy is a favorable candidate due to desirable properties such as high strength-to-weight ratio, exceptional thermo-mechanical stability and, minimum anisotropy relative to

BIKASH KUMAR and NAGAMANI JAYA BALILA are with the Department of Metallurgical Engineering and Materials Science, Indian Institute of Technology Bombay, Mumbai, Maharashtra 400076, India. Contact e-mail: bikash.kumar@iitb.ac.in
Manuscript submitted July 30, 2022; accepted December 2, 2022.
Article published online December 16, 2022

steels from microstructural-mechanical performance perspective.[14–17] In order to understand the full design potential of AM processed components, particularly for load bearing capacity in service condition, it is essential to provide the in-depth knowledge of the anisotropic tendency and to overcome this heterogeneity which may leads to deteriorations in alloy performance. Qiu *et al.* and Chen *et al.* were extensively studied 3D printed bulk Ti6Al4V alloy sample and observed insignificant difference in Young's modulus (*X*-plane:127 GPa, *Y*-plane: 128 GPa, *Z*-plane:127 GPa) and average hardness (*X*-plane: 4.5 GPa, *Y*-plane: 5 GPa, *Z*-plane: 5 GPa).[14,15] In addition to this, minor difference in microstructure was viewed for various planes for SLM Ti-alloy samples. In contrast, Ghaffari *et al.*, Kyvelou *et al.*, and other reaseraches obtained significant variation in microstructural characteristics and mechanical performance along different directions, and hence a marked anisotropic behavior, for additively manufactured steel alloys.[16,18] On the other hand, the nickel-based superalloy IN718 exhibits excellent mechanical properties with high oxidation and hot corrosion resistance at high temperatures.[19]

Among AM processes, DED technique, in particular, is known as near-net shaping technique that can produce parts by consolidating powder/filament in layer-by-layer fashion using focused laser heat source.[20] Extensive research was conducted on direct energy deposition (DED) processed IN718 and Ti6Al4V alloys to obtain process-structure–property characteristics.[21–23] Due to rapid heat dissipation from the base plate, the molten pool experiences high cooling rate (10^3 to 10^6 K/s) during the DED process.[24] Sufficiently high cooling rates cause the formation of metastable microstructure as well as residual stresses.[25] Parts fabricated using direct energy deposition technique are known to have complicated residual stress distributions which are usually undesirable. Rangaswamy *et al.* and Moat *et al.* mapped residual stress distribution in IN718 and SS316 alloy-based LENS® components, and Waspaloy parts, respectively, fabricated via DED technique using both neutron diffraction and contour methods.[26,27] Tensile stress was observed at the build wall edges because of relatively higher contraction at the edge as it was contributed by cooling as well as plastic deformation, whereas the central region exhibited compressive residual stress. The analogous stress profile for both material systems suggested that the origin of stress was thermal gradients and was independent of the metal used.[26] In contrast, Moat *et al.* reported tensile longitudinal stress at the top of deposited wall, while the stress gradually decreased towards the substrate over the build direction.[28] Wang *et al.*, predicted residual stress distribution for a 10-layered deposited SS410 steel alloy and drew comparable conclusions as suggested by Rangaswamy *et al.*[27] Influence of hatch length was critically studied by Bruno *et al.,* with a large gradient in residual stresses developing along the scan direction for longer hatch length sample, whereas, stress along build direction was found to be highly compressive for shorter hatch spacing.[29] Stress distribution by virtue of hatch length is influenced by the thermal gradients as well as changing solidification mechanisms. Generally, the as-printed part shows higher tensile stress field after its removal from the main fixture, however, inter-pass rolling technique can minimize the tensile residual stress as well as transform it into compressive stresses.[30]

Controlling the residual stress is non-trivial and can be governed by the several key factors, including substrate temperature, position of specimen, processing condition, scanning strategy, geometry of components, inter-pass dwell time, *etc.*[4,31–34] Denlinger *et al.* observed the reversal of residual stress behaviour upon employing dwell time between the successive passes during the fabrication of Ti-alloy and Inconel alloy build. Residual stress was increased by 80 and 122 pct for 20 and 40 seconds dwell time, respectively, as compared to without-dwell time condition in Ti-alloy, however the overall stress decreased by 12 and 23.5 pct for Inconel alloy, might be due to solid-state allotropic transformation in Ti-alloy.[34] Szost *et al.* concluded that the laser DED process deaccelerates the residual stress development as compared to the wire-arc DED process.[35] Additionally, substrate elimination in as-built condition would mitigates the residual stress at certain extent.[36] Part geometry and orientation are key factors that modify residual stress distribution in build structure.[37–39] Kruth *et al.* suggested that high scan speed and relatively low heat input can minimize tensile thermal stress.[39]

Adequate knowledge of the time–temperature field evolution in the molten region and HAZ is a prerequisite however, the complexities of the AM process due to the occurrence of several intricate phenomena at extremely high temperature makes experimentation and real-time monitoring impractical. Thus, researchers opted the numerical tools, and followed finite volume (FV) method, a finite difference (FD) method and finite element (FE) method approaches to predict the residual stress of the fabricated components accurately.[40–42] McMillan *et al.* developed a finite difference-based reduced-order simulation technique for the powder bed fusion process that can also be extended to the direct energy deposition (DED) technique.[41] Carmignani *et al.* established a 3D fully coupled thermo-mechanical model by assuming an elastic-viscoplastic material behaviour using a fully implicit time-integration approach to surpass the uncertain characteristics of the rate-independent constitutive model.[43] Keller *et al.* developed a multi-scale model for the fast prediction of residual stress and distortion by considering scan strategies and complex material behaviour through inherent strain approach.[44] In these limited attempts to simulate the thermal behaviour and residual stress in AM processes through FEM, the number of complex and stochastic examinations such as multilayer aspects, multi-material characteristics, real-time elastic–plastic response and parametric solidification study on successive layers and/or final part only limited literature provide insight into these factors exist. There is a requirement for a contemporary approach to link process control to application through a detailed understanding of thermo-mechanical characteristics.

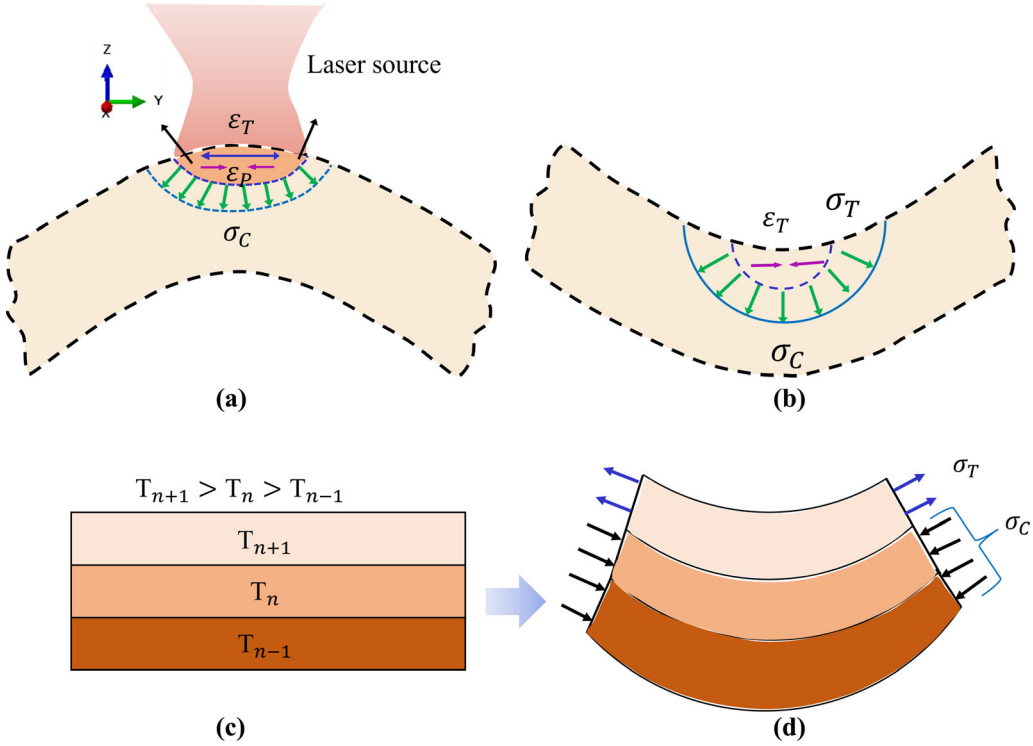

Fig. 1—Temperature gradient mechanism: (*a*) heating stage, (*b*) cooling stage; cooling mechanism: (*c*) heating stage, (*d*) cooling stage.[46] Where,ε_T and ε_p represents the thermal and plastic strains, respectively, σ_T and σ_C are the tensile and compressive stresses, respectively, T_{n-1}, T_n and T_{n+1} are the temperatures associated with $(n-1)$th, nth and $(n+1)$th layers, respectively. The image was reproduced with permission from Ref. [46].

Hence, it is evident that understanding the thermal stability, solidification behaviour, and origin of residual stress field would help in research intended for altering the engineering properties and improving the mechanical performance. To accurately predict these characteristics using a numerical simulation tool, the thermal and mechanical model must be coupled. In an attempt to handle these attributes, a two-step validation approach is conducted on a new model for single- (IN718-IN718) and multi-material (IN718-Ti6Al4V) systems. This model minimized the complexity of considering convective heat loss due to fluid flow by including linearly enhanced thermal conductivity and extended from scanty-to-long length multi-layered domain. The developed sequentially coupled thermo-mechanical model employs Python-Scripted-Interface for regulating MODEL CHANGE* feature to automate the process of layer-by-layer element activation and Fortran-based DFLUX subroutine for the application of Gaussian-based volumetric heat source in commercial software ABAQUS®6.14.

II. BACKGROUND: STRESS GENERATION MECHANISM IN AM

Thermal stresses arising due to a temperature gradient or solidification shrinkage contributes to the alteration in residual stress distribution. Thermal stresses are generated via: (a) temperature gradient mechanism (TGM) and (b) cool-down mechanism, which are illustrated schematically in Figure 1.[45,46] The TGM is employed to explain the stress evolution in single-track deposition, while the cool-down mechanism illustrates the stress development theory for the entire multilayered system. Figures 1(a), (b) schematically represents the TGM occurring during laser processing of sheet metal. The localized heating due to the laser beam creates a large temperature gradient across the thickness of the sheet metal. The thermal expansion of the HAZ is inhibited by the surrounding colder metal generating elastic compressive stresses in the HAZ. If the yield strength of the HAZ metal is exceeded, the HAZ accommodates the compressive strains by either plastic deformation or upsetting of the metal in the direction of heat source in absence of mechanical constraints as shown in Figure 1(a). The thermally stretched metal contracts on cooling, generating tensile stresses in the plastically deformed region, bending the metal away from the laser beam as depicted in Figure 1(b). In addition to SLM, the TGM is also applicable in selective laser sintering (SLS), where the underlying lower layers prevent the thermal expansion of the top layers.

The cool-down mechanism adopts the 'cooling' route to explain the introduction of residual stresses in a laser processed metal as follows.[46] The top molten layer possesses a relatively high temperature than the underlying layer as portrayed in Figure 1(c). This molten layer contracts to a large extent than the underlying layer on cooling and solidification. However, to maintain

structural equilibrium, this contraction is restricted by virtue of which tensile stress appears at the successive layer and reversal of stress state to compression occurs in the beneath layers as depicted schematically in Figure 1(d).[46]

III. MATERIALS AND METHODOLOGY

A. *Materials and Architecture*

Two alloy systems Ti6Al4V alloy and IN718 nickel-based superalloy were investigated in distinct configurations (Table I), as shown in Fig. 2. The configurations (10IN/IN & 1IN/Ti) differ in terms of process parameters, number of layers and substrate material (Table I). In nomenclature, the prefix represents the total deposited layers, while suffix signifies the build and substrate material. The *X*-, *Y*- and *Z*-axes were chosen as the scanning direction, width and build direction, respectively (Figure 2). Thermal stability, solidification behaviour and residual stress evolution in 10IN/IN and 10IN/Ti were extensively investigated, while 5Ti/Ti and 1IN/Ti were chosen for model validation. In order to maintain fidelity, horizontal parallel scan strategy were used in the deposition of each system.

The experimental conditions and process parameters used for the modeling were adopted from the literature presented in Table I and the methodology that Lia *et al.*, Mukherjee *et al.* and Shah *et al.* employed for part fabrication is briefly explained here.[40,47,48] The Ti6Al4V build was deposited over the Ti6Al4V substrate using powder fed into the laser beam for the 5Ti/

Table I. The Experimental Layout Opted for Sequentially Coupled Modeling

Build System	Substrate	Build Part	Total No. of Layers	Layer Thickness (mm)	Power (kW)	Beam Radius (μm)	Scan Length (mm)	Scan Velocity (m/s)	Dwell Time (s)
5Ti/Ti[40,48]	Ti6Al4V	Ti6Al4V	5	0.9	2	1500	150	0.0105	6
10IN/IN	IN718	IN718	10	0.67	0.6	800	16	0.004	0.0
10IN/Ti	Ti6Al4V	IN718	10	0.67	0.6	800	16	0.004	0.0
1IN/Ti[47]	Ti6Al4V	IN718	1	0.67	0.6	800	40	0.004	NA

Substrate thickness (mm): 10 (5Ti/Ti, 10IN/IN and 10IN/Ti) & 11 (1IN/Ti).

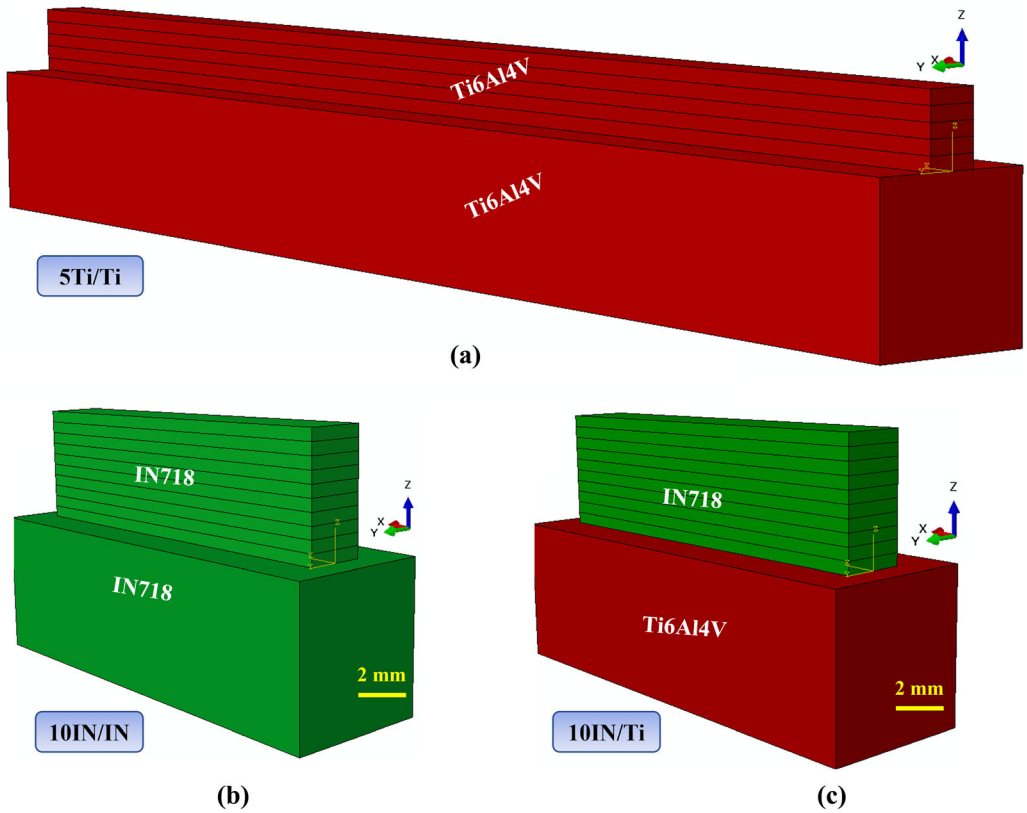

Fig. 2—Different configurations of the build system: (*a*) 5Ti/Ti, (*b*) 10IN/IN and (*c*) 10IN/Ti.

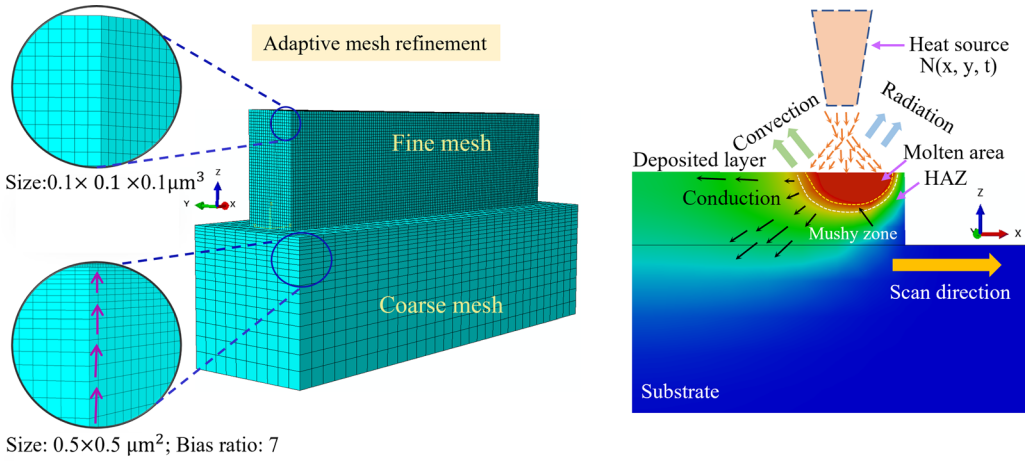

Fig. 3—(*a*) Adaptive mesh implemented over the solution domain during AM process modeling, (*b*) thermal boundary conditions applied for thermal analysis.

Ti system. The spherical Ti6Al4V powder (Phelly Materials) with mean particle size 127 μm (d_{10} = 77 μm and d_{90} = 187 μm) was produced *via* − 100/ + 325 mesh size.[40,48] The laser processing experiments were performed using IPG Model YLR-1200-C ytterbium fiber laser with a wavelength 1070 nm mounted with fiber optic delivery system having a diameter 200 μm. The temperature was experimentally measured using a K-type thermocouple located over the top of the substrate at mid-length of the deposit. In contrast, gas atomized Inconel 718 powder with an approximately spherical morphology, having average particle size of 53 to 150 μm was deposited onto a Ti6Al4V substrate for the fabrication of 1IN/Ti system. A 1.5 kW Laserline LDL 160–1500 diode laser, with 940 nm laser radiation operated in continuous mode, was utilized for the printing.[47] The residual stress measurements were conducted over the specimen in the post-machined condition using X-ray diffractometer (Bruker AXS D8). The (311) X-ray diffraction peak at 128.1 deg was chosen for the residual stress measurement using a $\sin^2\psi$ method, with tile angles from 0 to 45 deg.

B. *Modeling Assumptions and Assembly*

Several assumptions were made during transient heat transfer analysis and subsequent structural analysis to simulate the laser-based additive manufacturing processes. The surface of the whole solution domain was assumed to be flat and finite. The properties of the build and substrate part were assumed to be homogenous and isotropic. The laser heat source rendered a highly localized and collimated beam leading to a narrow melting path in the scan direction. Hence, adaptive mesh utility with DC3D8 element was imposed over the entire geometry to capture a steep temperature gradient. Accordingly, a fine mesh (0.1 × 0.1 × 0.1 μm^3) was employed over the build volume, which is in direct contact with the laser, whereas a coarse mesh (0.5 × 0.5 μm^2) with a bias ratio of 1:7 was used for the substrate section as shown in Figure 3(a). The heat losses due to conduction, convection and radiation are assigned as thermal boundary conditions as illustrated in Figure 3(b). Table II provides the detailed mesh specifications used for numerical modeling.

C. *Transient Heat Transfer Modeling*

The detailed descriptions of Fourier-based governing equation and thermal boundary conditions applied to carried out the transient heat transfer analysis over the 3D geometry are available elsewhere.[5,49] Convection was neglected during modeling since it has an insignificant effect on residual stress field generation.[9] Nevertheless, convective heat loss from the molten pool due to fluid flow considerably influences the transient thermal cycle beyond solidus temperature. Therefore, the thermal conductivity was assumed to increase linearly beyond solidus temperature by a factor of three.[50] The effect of liquid–solid transformation was included using the latent heat of fusion (Ti6Al4V: 360 kJ/kg, IN718: 197 kJ/kg) within the solidus–liquidus temperature range.[49,51]

An established Gaussian distributed double ellipsoidal volumetric heat source model was incorporated as the spatial and temporal distribution of the heat flux.[52] The optimized set of the double ellipsoidal heat source parameters used for analysis is presented in Table III. Thermal analysis was conducted during two stages: (a) movement of the laser beam and subsequent material deposition; (b) cooling down of the build system to ambient temperature after removal of thermal load. The convective heat transfer coefficients of 25 W m^{-2} K^{-1} and 18 W m^{-2} K^{-1} were allocated to the Ti6Al4V and IN718 alloy surfaces, respectively, in direct contact with steady air.[49,51] The radiative heat transfer coefficients

Table II. Detailed Mesh Specification Implemented in Numerical Simulation

Thermal Analysis			Sequential Coupled structural Analysis (Reduced Integration)		
Element Type	Elements	Nodes	Element Type	Elements	Nodes
DC3D8	117,760	128,298	C3D8R	117,760	128,298

Table III. Set of Double-Ellipsoidal Heat Source Parameters Used for Heat Transfer Modeling

Parameter	b	f_f	f_r	c	a_f	a_r
Value (mm)	0.5	0.6	1.4	1.0	1.0	1.0

for the Ti6Al4V and IN718 alloys were taken as 0.6 and 0.45, respectively.[49,51]

D. *Solidification Parameters Calculation*

The temperature gradient, G and solidification velocity, R are crucial parameters that govern the solidification behaviour of the IN718 alloy via control of the solute dispersion and, grain size and morphology. The G controls the heat flow direction that affects the grain size and orientation, whereas the R controls the solid–liquid interface morphology that governs the final microstructure.[53] The G is characterized by the temperature field developed by the laser source, while the R is associated with the beam velocity and the molten pool shape.[54] As mentioned earlier (Section III–C), only heat diffusion and convection (implemented as linearly increasing thermal conductivity) were considered. Neglecting the influence of mass feeding as well resulted in a simpler case of laser melting. To analyze the transformation in solidification behaviour for single- and multi-material build systems, the G at each location (x, y, z) within the molten pool was calculated using Eq. 1:[55]

$$G(x,y,z) = \left|\sqrt{[G_x(x,y,z)]^2+[G_y(x,y,z)]^2+[G_z(x,y,z)]^2}\right|, \quad [1]$$

where G_x, G_y and G_z are the temperature gradients along the x, y and z directions. The R is determined through the transient behaviour of temperature given by Eq. [2][56]:

$$R = \frac{1}{G} \times \frac{\mathrm{d}T}{\mathrm{d}t^*}, \quad [2]$$

where $\mathrm{d}T/\mathrm{d}t^*$ represents the temperature transition, $\mathrm{d}T$ with change in time $\mathrm{d}t^*$.

Solidified dendritic microstructures provide various characteristic length scales such as primary and secondary dendritic arm spacing (PDAS & SDAS). The PDAS which is an extensive function of G and R has a critical role in the permeability of the mushy zone (semi-solid region) and influences the defect appearance such as solidification crack. The expected PDAS measure (δ_{PDAS}) was predicted by the Kurz–Fischer[57] and Trivedi[58] models given by Eqs. [3] and [4], respectively:

$$\delta_{PDAS} = 4.3(\Delta T_{L-S})^{0.5}\left[\frac{D_l \Gamma}{\Delta T_o P_c R}\right]^{0.25} G^{-0.5} R^{-0.25}, \quad [3]$$

where ΔT_{L-S} and ΔT_o are the non-equilibrium (200 K) and equilibrium (105 K) solidus–liquidus temperature range for IN718.[55] D_l and Γ are the liquid diffusion coefficient (3×10^{-9} m^2/s) and Gibbs–Thomson parameter (1×10^{-7} K.m), respectively.[59] P_c is the partition coefficient (0.48 for IN718).[59]

$$\delta_{PDAS} = 2.83(hD_l \Gamma \Delta T_o P_c)^{0.25} G^{-0.5} R^{-0.25}, \quad [4]$$

where h is harmonic perturbation coefficient assumed as 28.[58]

E. *Structural Modeling*

A sequential coupled thermo-mechanical model was proposed to monitor the deposition-induced residual stress field in real-time. The time–temperature history calculated through the heat transfer model is imported into a predefined field as an input load for mechanical modeling. Since inertia has a negligible effect on the mechanical response during metal deposition on the substrate, static stress analysis was conducted in the current study. The mechanical behaviour of the build systems was governed by the infinitesimal strain theory. The force equation in static equilibrium in accordance with the Lagrangian reference frame is given by Reference 49:

$$\frac{\partial \sigma_{ij}}{\partial x_j} + bf_i = 0, \quad [5]$$

where σ_{ij} is the Cauchy stress tensor and bf_i is the total body force vector.

Since the stress tensor is symmetric in nature:

$$\sigma_{ij} = \sigma_{ji} \quad [6]$$

The total strain, ε_{ij}^t was expressed as the sum of the all the discrete elemental strain components that contributed to the residual stress development:

$$\varepsilon_{ij}^t = \varepsilon_{ij}^{el} + \varepsilon_{ij}^{th} + \varepsilon_{ij}^{cr} + \varepsilon_{ij}^{pl} + \varepsilon_{ij}^{pt} + \varepsilon_{ij}^{vp} + \varepsilon_{ij}^{vol}, \quad [7]$$

where ε_{ij}^{el}, ε_{ij}^{th}, ε_{ij}^{cr}, ε_{ij}^{pl}, ε_{ij}^{pt}, ε_{ij}^{vp} and ε_{ij}^{vol} describe the elastic, thermal, creep, plastic, phase transformation-induced plasticity, viscoplastic and volumetric strains. However,

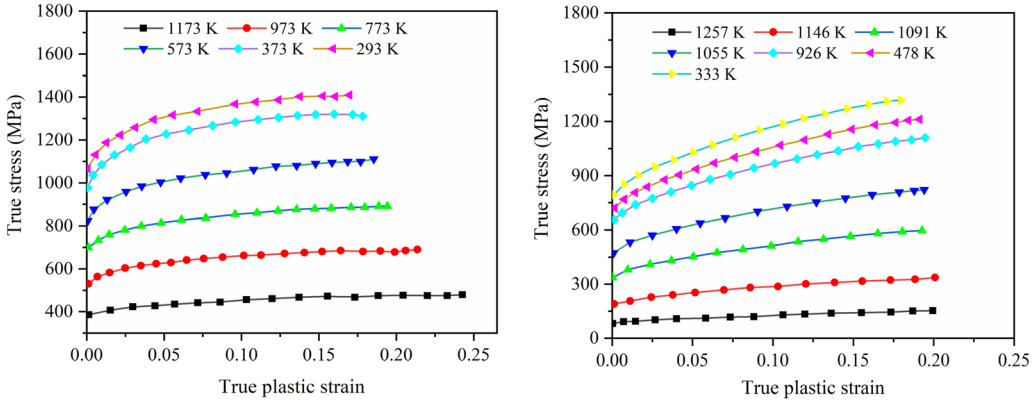

Fig. 4—Temperature-dependent true stress vs strain plots for (*a*) Ti6Al4V alloy, (*b*) IN718 alloy used to describe corresponding plastic response in numerical analysis.[60,61] The image was reproduced with permission from Refs. [60,61].

the creep, phase transformation-induced plasticity, viscoplastic and volumetric strains were neglected due to insignificant contribution to residual stress generation.[49]

The elastic behaviour of the build systems was incorporated using Hooke's law with elastic modulus and Poisson's ratio varying as a function of temperature. Plasticity was governed by the von Mises yield criterion and isotropic Prandtl–Reuss hardening rule with plastic strains corresponding to a temperature-dependent yield stress is presented in Fig. 4. The experimental true stress–strain curves corresponding to the strain rate of 0.01 s^{-1} was considered from the literature.[60,61] The thermal strain was determined using the thermal expansion coefficient and temperature variation. Thus, the overall constitutive equation used for the calculation of the thermo-elastic–plastic response during metal deposition over the different substrates is described as follows:

$$\varepsilon_{ij}^{t} = \frac{1+\mu}{\mathrm{E}_m}\sigma_{ij} - \frac{\mu}{\mathrm{E}_m}\sigma_{ij}\delta_{ij} + \lambda S_{ij} + \alpha_m(T - T_i)\delta_{ij}, \quad [8]$$

where μ, E_m, σ_{ij}, δ_{ij},λ, S_{ij}, α_m are the Poisson's ratio, elastic modulus, flow stress, Kronecker delta, plastic flow factor, and deviatoric stress factor, thermal expansion coefficient, respectively. λ is zero in the elastic region, and is greater than zero in the elastic–plastic regime. T and T_i are the instantaneous and ambient temperatures, respectively. The Prandtl-Reuss hardening rule is expressed as:

$$\varepsilon_{ij}^{pl} = \lambda S_{ij} \quad [9]$$

The elemental participations were compiled to form a global set of equations, which were then solved to determine the state variables for each nodal point in an eight-node brick element. The mechanical model utilized the time–temperature database for calculating the displacement field in the form of strain increment. Globally, the strain increment can therefore be disintegrated into contributing strain components as follows:

$$\mathrm{d}\varepsilon^{\mathrm{t}} = \mathrm{d}\varepsilon^{\mathrm{el}} + \mathrm{d}\varepsilon^{\mathrm{pl}} + \mathrm{d}\varepsilon^{\mathrm{th}} \quad [10]$$

Considering the von Mises yield criterion and Prandtl-Reuss hardening rule, the incremental stress, $d\sigma$ was expressed as[62]:

$$\mathrm{d}\sigma = \left|D^{\mathrm{el-pl}}\right|\mathrm{d}\varepsilon - \left|C^{\mathrm{th}}\right|\mathrm{d}T \quad [11]$$

$$\left|D^{\mathrm{el-pl}}\right| = \left|D^{\mathrm{el}}\right| - \left|D^{\mathrm{pl}}\right| \quad [12]$$

$$\left|C^{\mathrm{th}}\right| = \{\alpha\}\left|D^{\mathrm{el}}\right|, \quad [13]$$

where $\left|D^{\mathrm{el-pl}}\right|$ represents the elasto-plastic matrix, $\left|D^{\mathrm{el}}\right|$, $\left|D^{\mathrm{pl}}\right|$ and $\left|C^{\mathrm{th}}\right|$ are the elastic, plastic and thermal stiffness matrices, respectively. $\mathrm{d}T$ is the temperature increment. The elasto-plastic matrix, $\left|D^{\mathrm{el-pl}}\right|$ is given by:

$$\left|D^{\mathrm{el-pl}}\right| = \left[\left|D^{\mathrm{el}}\right| - \left|D^{\mathrm{el}}\right|\frac{\partial f}{\partial \sigma}\left(\frac{\partial f}{\partial \sigma}\right)^{\mathrm{T}}\left|D^{\mathrm{el}}\right|\frac{1}{3H + E_{\mathrm{m}}}\right], \quad [14]$$

where the function, f is the yield locus and H is the shear modulus.

The von Mises yield stress, σ_v was calculated as:

$$\sigma_v = \sqrt{\frac{1}{2}\left[(\sigma_1 - \sigma_2)^2 + (\sigma_2 - \sigma_3)^2 + (\sigma_3 - \sigma_1)^2\right]}, \quad [15]$$

where σ_1, σ_2 and σ_3 are the principal stresses.

IV. RESULTS AND DISCUSSION

Figure 5 shows the comparison between the calculated and corresponding experimentally measured time–temperature profile at the build-substrate interface for Ti6Al4V metal deposition on the Ti6Al4V substrate, i.e., 5Ti/Ti defined in Table I. Besides, the 3D isothermal contour is also presented to analyze the spatial

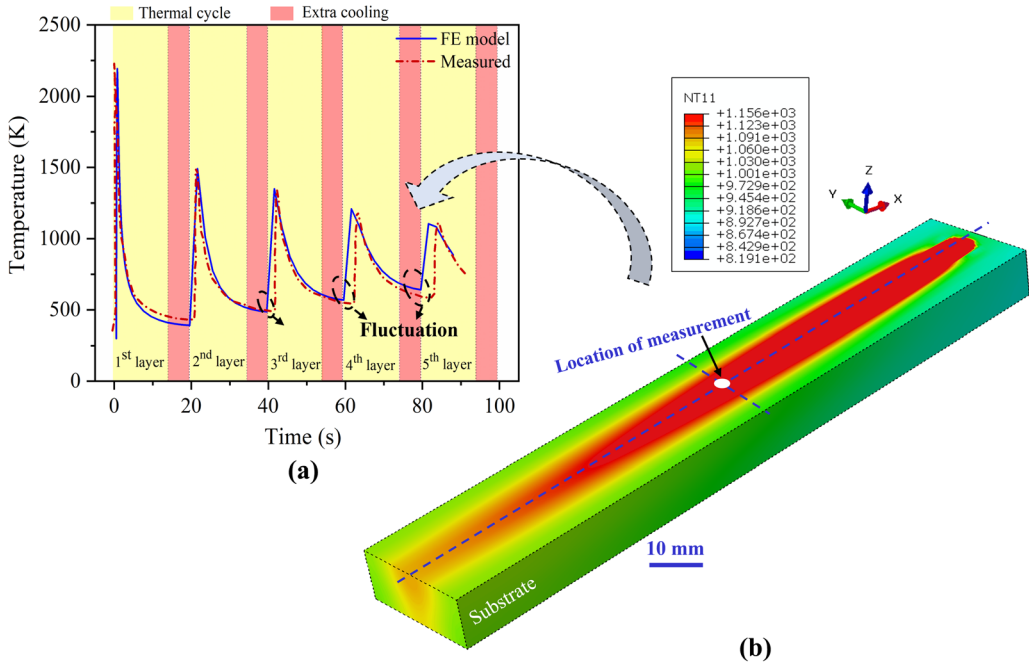

Fig. 5—(*a*) Comparison between experimentally measured[40] and numerically predicted thermal behaviour of laser-assisted AM 5Ti/Ti. (*b*) 3-D temperature distribution contours over the system. The mid-width, mid-length section of the build-substrate interface (white circle) was the location chosen for monitoring the temperature distribution. The image 5 (a) was reproduced with permission from Ref. [40] and used for validation.

distribution of temperature after the deposition of five-layers. A qualitative agreement between the predicted and experimental measured thermal cycle confirms the robustness of the developed heat transfer model for simulating the laser-assisted additive manufacturing process. In order to maintain the consistency between experimental and numerical results, a time lag of 6 seconds (indicated as a red band) was introduced between two subsequent track depositions. Experimental determination of the transient temperature behaviour of the depositing material is quite challenging. Therefore, a thermocouple-based conventional technique was used to capture the thermal cycle.[40]

The maximum temperature of 2245 K was attained at the interface after the deposition of the 1st layer. However, this temperature decreased gradually to 1500 K, 1450 K, 1260 K and 1160 K over the 2nd, 3rd, 4th and 5th layer, respectively. Gradual contraction in the thermal cycle was clearly seen in the deposition of a new layer. As the heat source moved away from the substrate in the direction of build height, the temperature experienced by the interface decreased due to reduced heat diffusion from the upper to its underlying layer. Similar trends in the interface temperature were also observed by other researchers.[40,63] Calculated time–temperature history at the end of the cooling stage began deviating from the experimental measurements after deposition of the 2nd layer, marked as a black dashed circle in Fig. 5. The increased cooling times of 1, 2, and 3 seconds required for 3rd, 4th and 5th layer depositions, respectively, during experiments could not be captured numerically. This discrepancy was attributed to inappropriate thermal boundary conditions or heat transfer coefficient used in the FE model.

Figure 6(a) shows the non-uniform spatial temperature distribution during the metal deposition of the odd 1st, 3rd, 5th and 7th layers of IN718 on an IN718 substrate for the 10IN/IN. The temperatures over the whole solution domain are rendered by color contours, where the grey band represents the region with the highest temperature range of 1858 K to 2318 K ($> T_{melt}$). The back plate or substrate on which the metal layers were deposited acted as a heat sink. Hence, the molten pool obtained for 1st layer was highly localized, and gradually increases with build height. Simlar observation has been confirmed by Kempen *et al.* and other researchers in their study.[31,64,65] Manvatkar *et al.* (a, b) found comparable results during experimental and numerical investigation and concluded that the 1st layer could effectively diffuse heat into the substrate because the substrate was initially at ambient temperature and had a tendency to absorb heat efficiently because of the heat sink effect.[64,65] The thermally affected regions, molten/fusion zone (FZ), mushy zone (MZ), HAZ; developed by virtue of the non-uniform temperature distribution is illustrated in Figure 6(b). The reheating of the underlying layer due to the deposition of the successive layer is also indicated. The mushy zone (bounded by dashed black lines) is constrained within the solidus (1533 K) and liquidus (1609 K) temperatures.

To understand the effect of multi-layer deposition on melt pool profile, the bead profile across the scanning direction at the middle section of each layer is superimposed and illustrated in a single frame in Figure 6(c) for

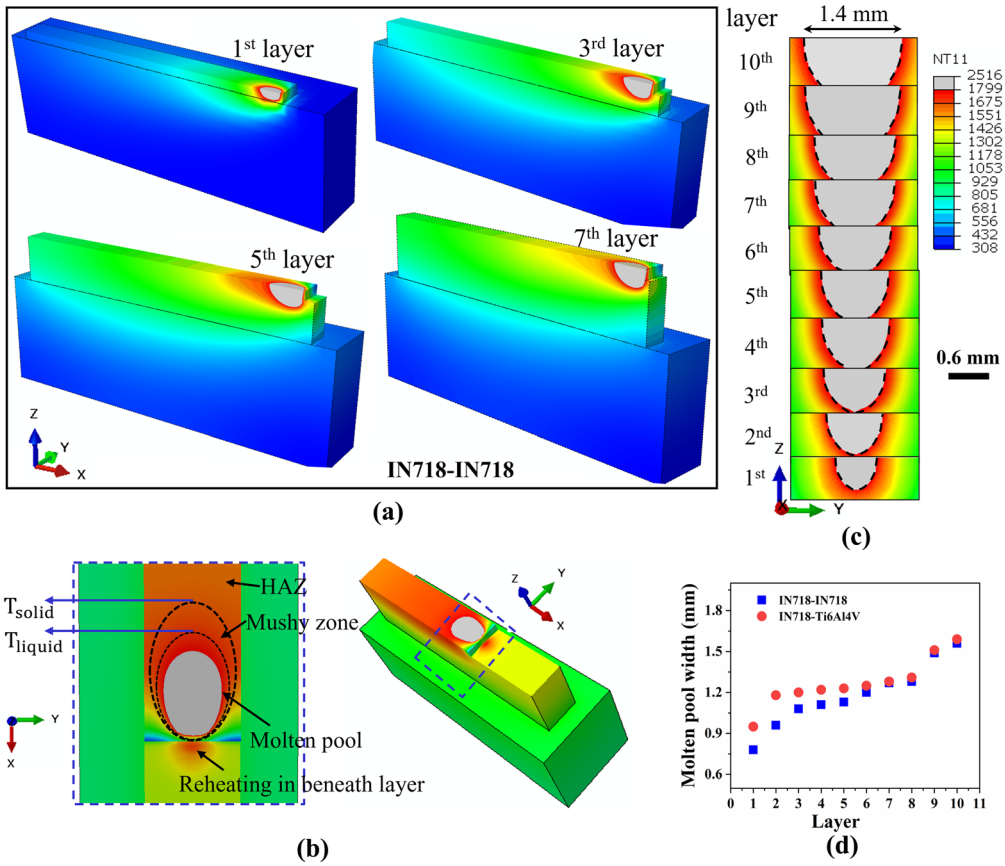

Fig. 6—Bead analysis: (*a*) 3D temperature contours after 1st, 3rd, 5th and 7th layer deposition in 10IN/IN; (*b*) 2D and 3D temperature contours of thermal zones during deposition, (*c*) 2D temperature contours across the 10IN/IN bead, (*d*) Molten pool widths at different layers of 10IN/IN and 10IN/Ti.

10IN/IN. Gradual increase in melt pool size is attributed to the poor effect of heat sink towards increasing build height. The conduction mode of heat transfer prevails over the convection mode for initial layers due to the strong cooling effect of the substrate however, as the building height increased far from the substrate, the convection mode became effective. Therefore, the lower layer experienced a high rate of heat dissipation than the top layer. This could have caused wall thickness and increase in melt pool size for the top layer in comparison to the bottom layer. Similarly, Kistler *et al.* found the melt pool broadening and fusion zone shape transformation upon increasing normalized latent heat for single IN718 bead deposition on ambient and pre-heated 718 substrates.[21] In a parallel study, Grange *et al.* explained that high accumulation of energy results in a larger melt pool and a deeper mushy zone due to low temperature gradient.[66]

The variation of melt pool size in each layer for 10IN/IN and 10IN/Ti is presented graphically in Figure 6(d). The insignificant difference in melt pool sizes, 1.56 and 1.58 mm in the 10th layer for build 10IN/IN and 10IN/Ti, respectively, indicates that the influence of the substrate is negligible at higher layers. Nevertheless, the melt pool size was found to be sensitive at the lower layers. Melt pool sizes of 0.78 and 0.96 mm were obtained at 1st and 2nd layer for IN718 substrate (10IN/IN). On the other hand, the melt pool sizes were 0.95 and 1.18 mm for Ti6Al4V substrate (10IN/Ti). Relatively high thermal conductivity of IN718 (13 W/m K) allowed rapid rate of heat extraction, while high temperatures last longer in the deposited metal in the Ti6Al4V substrate (10IN/Ti) because of the low thermal conductivity (7 W/m K). The influence of substrate is effective up to the 5th layer beyond which approximately similar melt pool sizes formed in both systems [Figure 6(d)].

Figure 7 shows the calculated thermal cycles at six monitored locations, each at the mid-length and mid-width of the 1st and alternate even 2nd, 4th, 6th and 8th layers in the 10IN/IN. Each thermal cycle contains the expected recurrent spikes. In each of them, the first spike represents the peak temperature corresponding to the laser beam positioned just above the monitored location and the other subsequent spikes correspond to the laser positioned above the monitored locations for the successive passes. Hence, the thermal cycles are an appropriate representation of the progress of the deposition process. The peak temperature gradually increased from 2278 K to 2510 K for the 2nd layer to the 10th layer, respectively, due to the accumulation of retained heat at the terminal stage of each cycle. This lead to higher temperatures for deposition of successive layers. Heat accumulated during each thermal cycle, as

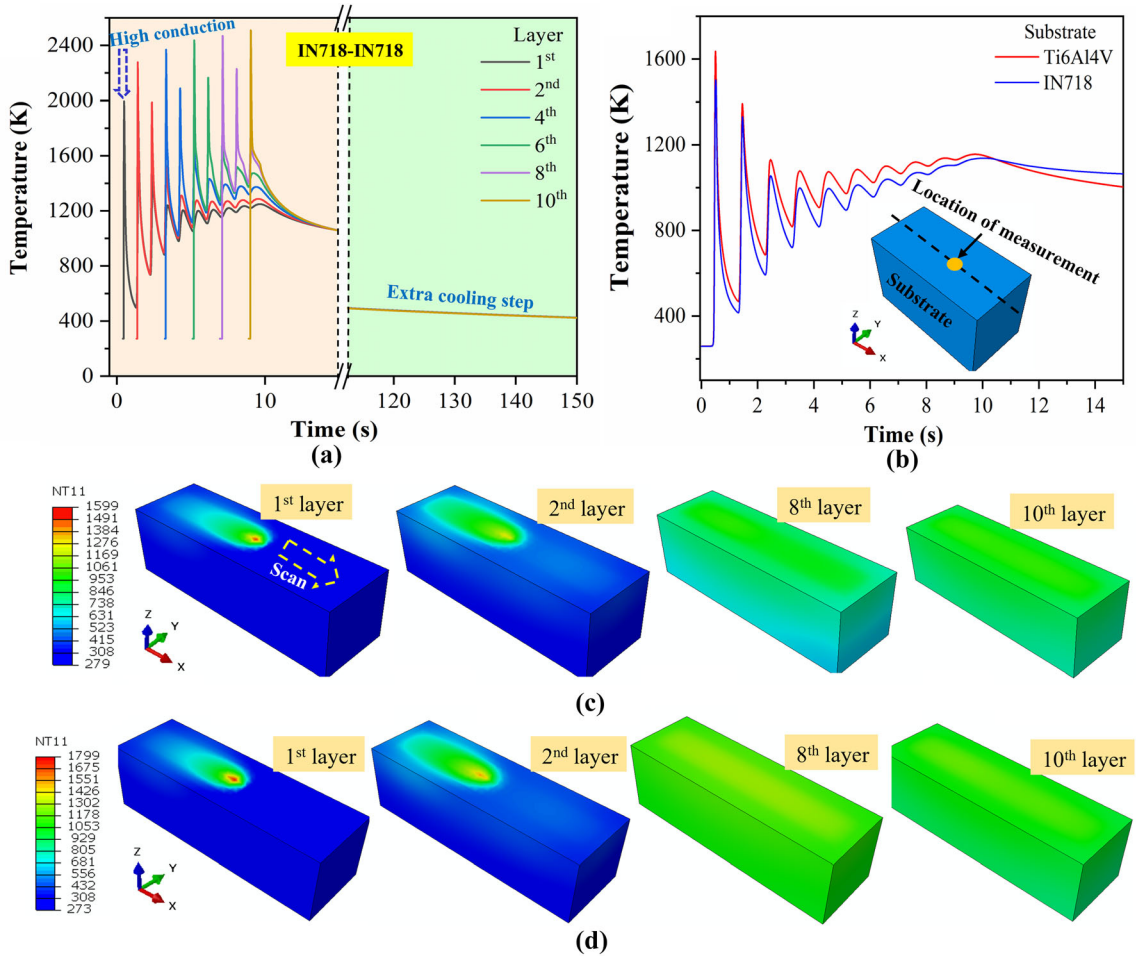

Fig. 7—(*a*) Thermal cycles at the 1st and even layers deposited in 10IN/IN, (*b*) Thermal cycles captured at mid-length and mid-width location of IN718 (10IN/IN) and Ti6Al4V (10IN/Ti) substrate. 3D temporal temperature contours after the 1st, 2nd, 8th and 10th layer depositions in (*c*) 10IN/IN and (*d*) 10IN/Ti.

the temperature never reached ambient values at the end of the cycle [Figure 7(a)].

The solidification rate for the first layer is relatively higher as compared to the other consecutive layers due to the adjacent initially cold substrate. This caused the temperature rise from the 1st to the 2nd layer to be 317 K, while being only 91 K from the 2nd to the 4th layer. A similar pattern of thermal cycle, showing a significant dip in the temperature profile during the deposition of the 1st layer as compared to other successive layers, was also noted by other groups irrespective of materials and similar interpretations as explained here were mentioned for this finding.[27,40] The extra cooling time of 100 seconds was provided during the simulation in order to cool the system down to room temperature. Figure 7b shows the thermal cycles obtained at the mid-length and mid-width of the IN718 (10IN/IN) and Ti6Al4V (10IN/Ti) substrates after the 10 layer deposition of IN718. The temperature evolution for the Ti-alloy was observed to be higher due to lower heat dissipation (thermal conductivity). The 3D contour-based temporal temperature distributions over the IN718 and Ti6Al4V substrate are shown in Figures 7(c) and (d), respectively. Replacement of IN718 substrate with Ti6Al4V alloy produced significant difference in maximum temperature ($\sim$ 220 K). This difference is sufficient to trigger the solidification behaviour, residual stresses as well as internal defects (porosity, hot-crack) during the direct energy deposition process in the system 10IN/Ti.

Figure 8a exhibits the peak temperatures at the mid-length and mid-width position of each deposited layer when the laser beam is positioned at the monitored locations of 10IN/IN and 10IN/Ti. The significant difference in peak temperature seen between 10IN/IN and 10IN/Ti at the 1st layer could be due to the substantial change in thermo-physical properties of the IN and Ti substrates. Subsequently, the temperature difference decreased up to the 5th layer followed by overlapping of peak temperatures due to reduced influence of the substrates for both the systems. Thus, the substrate acts as a heat sink up to the 5th layer for the set of parameters chosen in the present study.

Figure 8b shows the temperatures across the scan direction at 0.2, 0.4, 0.6 and 0.8 mm from the heat source. Owing to the localization of heat flux, the maximum temperature is confined to the domain immediately adjacent to the laser source, while distant

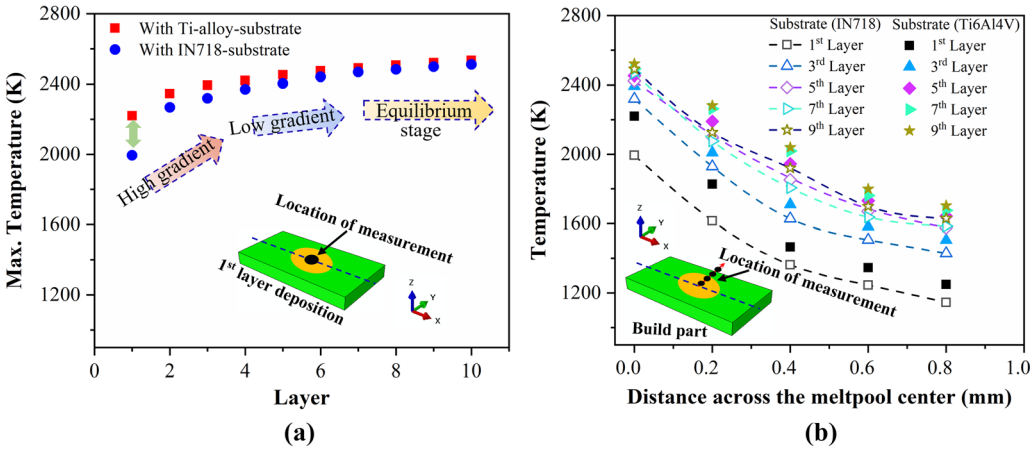

Fig. 8—(*a*) Maximum temperature at the middle of each deposited layer, (*b*) Temperature across meltpool center with laser at zero (scan line), 0.2, 0.4, 0.6 and 0.8 mm away in 10IN/IN and 10IN/Ti.

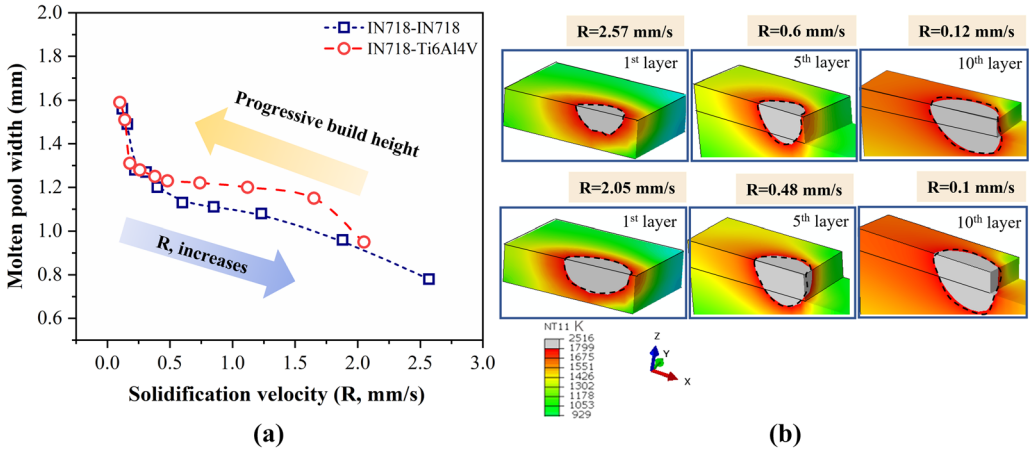

Fig. 9—(*a*) Variation of melt pool width with solidification velocity over the 10IN/IN and 10IN/Ti, (*b*) 3D temperature contours of the melt pools in the 1st, 5th and 10th layers at different solidification velocities in 10IN/IN (1st row) and 10IN/Ti (2nd row).

locations remain at relatively low temperatures. The investigated locations in the successive layers experienced relatively higher temperatures due to the widening of the melt pool with build height. Changing the substrate from IN718 to Ti6Al4V was reflected only up to the initial 5 layers after which the calculated temperature difference was indistinguishable for both systems.

The solidification velocity, R is related to the laser scan speed as well as melt pool shape and can control the development of interface morphology as indicated by several researchers.[54,56] To understand the effect of solidification velocity on progressive building, the melt pool dimensions are plotted against the corresponding solidification velocity for each layer in Figure 9(a). The predicted R follows a non-linear serpentine trend for 10IN/Ti systems. The R for five-layers beginning from substrate surface was determined to be 2.57, 1.88, 1.23, 0.85 and 0.6 mm/s for 10IN/IN, whereas, 2.05, 1.65, 1.12, 0.74 and 0.48 mm/s for 10IN/Ti.

The higher residual thermal energy available at the last deposited layer reduced the solidification velocity by maintaining the melt pool for a longer time. Hence, increased melt pool sizes and decreased solidification velocities are attained at higher build height. Ti6Al4V alloy substrates retained higher temperatures for a relatively longer duration causing larger melt pools and lower solidification velocities during the fabrication of initial 5 layers. In concurrent research by Qi *et al.* and Mazumdar *et al.*, a comparable trend of solidification velocity variation was noticed upon altering heat input.[67,68] It was explained that motion of molten metal within a melt pool is largely governed by the Marangoni force due to variation in surface tension because of a spatial temperature gradients. Figure 9(b) exhibits the melt pool modification accompanied by varied solidification velocities attained in the 1st, 5th and 10th layers for 10IN/IN (1st row) and 10IN/Ti (2nd row). A change in the melt pool on changing the substrate material as well as depositing the 1st to the 5th

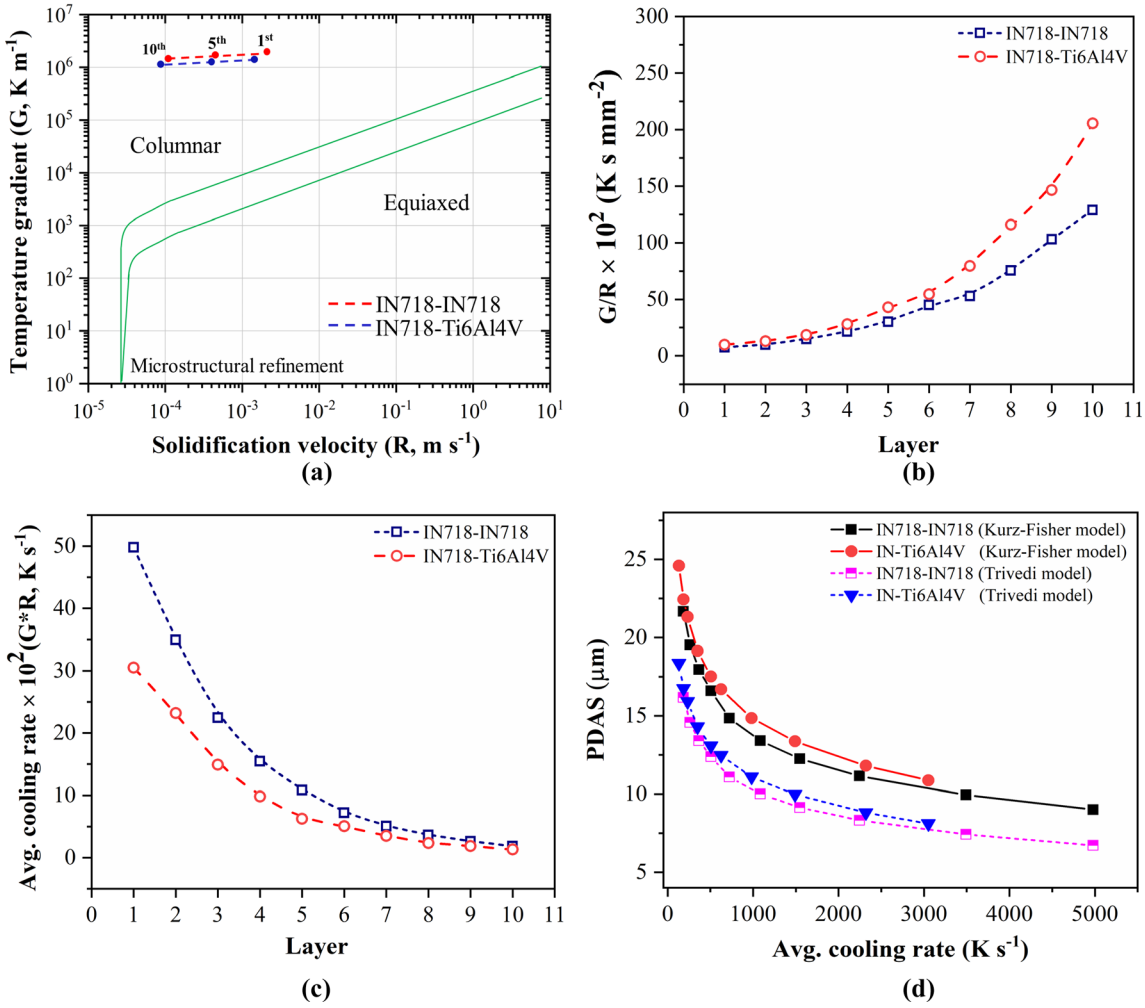

Fig. 10—(*a*) Superposition of the calculated G and R of the 1st, 5th and 10th layer on the solidification map, (*b*) G/R, (*c*) Average cooling rate, $G \times R$ variation with deposited layers, (*d*) Primary dendritic arm spacing (PDAS) vs. average cooling rate in the 10IN/IN and 10IN/Ti.

layer is expected. However, the differences were indistinguishable for the top 10th layer.

The size and morphology of solidified microstructure can be predicted as either columnar, equiaxed or mixed by plotting the temperature gradient, G versus the solidification velocity, R in the standard solidification map shown in Figure 10(a).[69] The G and R values were calculated as 1.93×10^6, 1.81×10^6 and 1.54×10^6 K/m and 0.00257, 0.0006 and 0.00012 m/s, respectively, for the 1st, 5th and 10th layers of the 10IN/IN (red), and 1.48×10^6, 1.30×10^6 and 1.21×10^6 K/m and 0.00205, 0.00048 and 0.0001 m/s, respectively, for 10IN/Ti. Incorporating these values into the solidification map to gain insights into the microstructural morphology reveals that the data predicts a columnar microstructure on liquid-to-solid transformation. Several studies showed that different additively manufactured alloy systems often observed columnar grain along the build direction confirming the reliability of the semi-quantitative data obtained from the current model.[21,23,24] Figure 10(b) shows the G/R ratio obtained in each layer for both 10IN/IN and 10IN/Ti. Although the solidification parameters predicted columnar growth for each layer, the changing CTE can induce a columnar to equiaxed structure transition, which is higher for initial layers with low G/R values. The solidification mode shifts from planar to cellular and cellular to dendritic (cellular/columnar/equiaxed) with increasing R.[54,55,70] Figure 10c illustrates the product $G \times R$ characterizing the average cooling rate experienced by each layer during build fabrication. The cooling rates were determined as 4980, 1086 and 185 K/s for the 1st, 5th and 10th layer for the IN718 substrate system, and 3050, 624 and 131 K/s, respectively, for the Ti6Al4V substrate system. The decrease in cooling rate upon increasing build height is interlinked with the R and melt pool size. Higher R and cooling rate allow shallow or small melt pool since molten pools last for a shorter duration due to the rapid heat diffusion rate. The cooling rate also governs microstructural features such as the PDAS and SDAS that directly influence the mechanical properties of individual grains.[71] The expected PDAS using the Kurz-Fischer[57] and Trivedi models[58] are plotted against the corresponding average cooling rate [Figure 10(d)]. The PDAS were calculated as 10.8 to 24.6 μm for the 10IN/Ti, and 8.9 to 21.65 μm

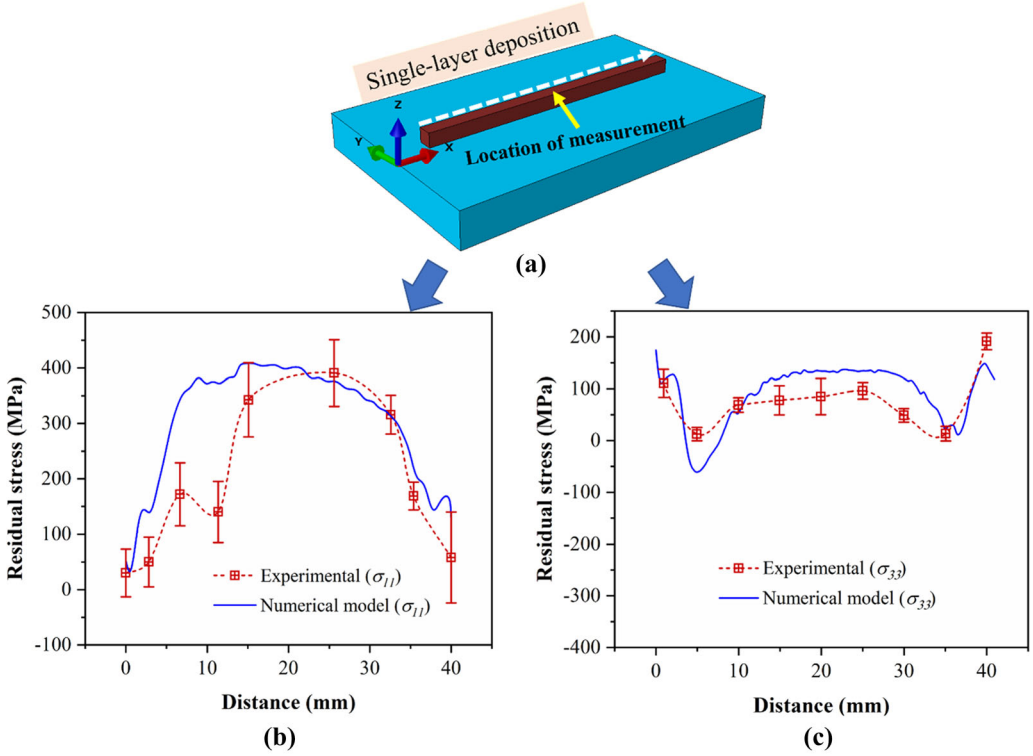

Fig. 11—(*a*) Illustration of stress measurements location (in Fig. b, c) for 1IN/Ti multi-material system along deposition direction, comparison of experimentally measured[47] and numerically calculated residual stress (*b*) σ_{11} and (*c*) σ_{33} in 1IN/Ti system. The image 11 (b) and (c) was reproduced from Ref. [47] under the terms of the creative commons attribution CC BY license, and used for validation.

for 10IN/IN as portrayed in Figure 10(d). It indicates a continuous increase in PDAS along the build direction in both 10IN/IN & 10IN/Ti due to reduction in cooling rates towards the top layer. The high cooling rate at the substrate provided insufficient time for grain coarsening or dendritic growth leading to smaller arm spacings. The numerically predicted variation of cooling rate and resulting PDAS due to change in accumulated thermal energy for different substrates is in qualitative agreement with that of the experimental output, as presented in the published research works on stainless steel and Titanium aluminides.[72,73]

While the temperature distribution is the key factor responsible for the generation of residual stresses in a homogenous material, change in thermal expansion coefficient (ΔCTE) is the main culprit in multi-material deposition systems. Warping of the final part and crack formation are the major concerns that arise due to life-limiting residual stresses. The sequential coupled model was also developed to understand the mechanism of residual stress generation in a multi-material system and validated with experimental results in this section. Figures 11(a) and (b) compare the experimentally measured[47] longitudinal stress, σ_{11} and through-thickness stress, σ_{33} with numerically calculated stress components for the single layer IN718 alloy deposition on the Ti6Al4V substrate (1IN/Ti). Single layers of IN718 were deposited on Ti6Al4V substrate using different powder mass flow rates by laser DED with the 1.5 kW diode laser operating in continuous beam mode. The residual stress was calculated by assuming an elastic modulus of 200 GPa and Poisson's ratio of 0.30.[47] A fair agreement and similar trends are observed in terms of magnitude and stress distribution between them. The maximum longitudinal and through-thickness residual stresses, σ_{11} & σ_{33} measured using an experimental technique (X-ray diffraction, $\sin^2\psi$ method) were 390 ± 55 MPa and 110 ± 20 MPa, respectively,[47] whereas 401 and 178 MPa, respectively, were calculated from the developed model. The stresses were measured at different locations along the scan direction in order to check for repeatability and determine the error bar.[47] The mismatch in the distribution and magnitude of the σ_{11} and σ_{33} components between the measured and calculated values could be due to measurement complexity, non-uniform sample clamping forces and assumptions made during modeling. The von Mises stress also extracted from the modeling was ~ 400 MPa indicating that the major contribution comes from longitudinal stress component, σ_{11}.

Figures 12(a) and (b) exhibit contours of the longitudinal residual stress, σ_{11} distribution that were generated after the deposition of two layers in 10IN/IN and 10IN/Ti, respectively. Further, Figure 12(c) and (d) show the 2D residual stress profiles corresponding to Figures 12(a) and (b) captured at the mid-width along the build height starting from the bottom of the substrate (indicated by a black dashed arrow). The maximum σ_{11} located near the top of the 2nd layer was

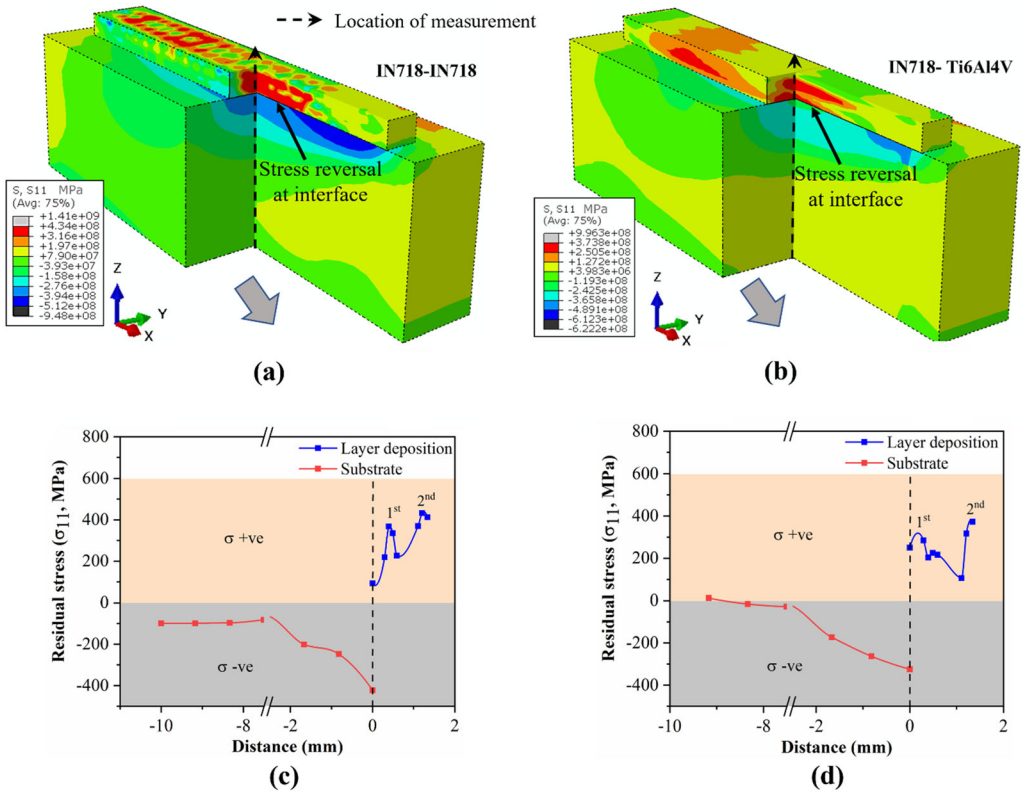

Fig. 12—3D contours of the residual stress component, σ_{11} after 2nd layer deposition in (*a*) 10IN/IN and (*b*) 10IN/Ti.

432 MPa, which decreased rapidly with depth to ~ 220 MPa near the bottom of the 2nd layer. The σ_{11} abruptly increased to 367 MPa at the top of the 1st layer, which again decreased rapidly with depth to ~ 100 MPa at the interface. High compressive stresses ~ 422 MPa were generated in the substrate near the interface that reduced to ~ 80 MPa and then stabilized at ~ 100 MPa in the 10IN/IN. The 10IN/Ti exhibited similar trend in both the layers and the substrate albeit at smaller absolute values. The maximum σ_{11} located at the top of the 2nd layer was ~ 372 MPa, which decreased abruptly with depth to ~ 100 MPa near the top of the 2nd layer. This drop was followed by a rapid increase to ~ 284 MPa with increasing depth to near the top of the 1st layer, which again decreased with depth to ~ 260 MPa at the interface. High compressive stresses ~ 320 MPa were generated in the substrate at the interface that reduced to ~ 20 MPa and then stabilized at ~ 10 MPa in the 10IN/Ti.

During the deposition of 1st layer, both the deposited metal and IN718 substrate were heated up extensively and a substantial expansion occurred along the scanning direction (*X*-axis). The mechanical constraint of the IN718 substrate inhibited the expansion caused by the compressive residual stress of ~ 422 MPa in the substrate and tensile residual stresses of 367 and 432 MPa at the top of the 1st layer and near the top of the 2nd layer, respectively. In contrast, lower σ_{11} of 372 and 284 MPa were found at the top of the 2nd and 1st layers, respectively, followed by compressive stress of 320 MPa in the Ti6Al4V substrate for 10IN/Ti. The Ti6Al4V substrate reduced the thermal gradient between the substrate and 1st deposited layer by maintaining high temperature for a relatively longer time span by virtue of low thermal conductivity. Since the deposited metal was not cooled up to room temperature, the ΔCTE effect was negligible despite being a multi-material system. Therefore, the temperature gradient is the only prevalent factor for the generation of residual stress in both systems. The high thermal gradient developed in 10IN/IN relative to 10IN/Ti caused the generation of high residual stresses. When the 2nd layer or the top layer is deposited, the underlying layer which already cooled down to some extent experienced reheating effect due to heat diffusion. This resulted in stress alleviation up to a certain extent leading to relatively lower tensile residual stresses in the underlying layer. The findings agree with those reported by earlier investigations.[26,28,40] For instance, Moat *et al.,* Mukherjee *et al.,*and other researchers saw stress release upon depositing successive layers onto layers below them, owing to reheating or remeting phenomena and they claimed that the stress developed at the layer below could be released and even transformed into compressive state in the post heating process of successive layers.[27,28] This is an unintended yet desirable component of additive layer-by-layer manufacturing that it allows for such *in-situ* heat treatment.

Figure 13 shows the variation in residual stresses, σ_{11} and corresponding temperature distributions in 10IN/IN and 10IN/Ti after cooling. An extra cooling time of 100 s was provided after the deposition of 10 layers for

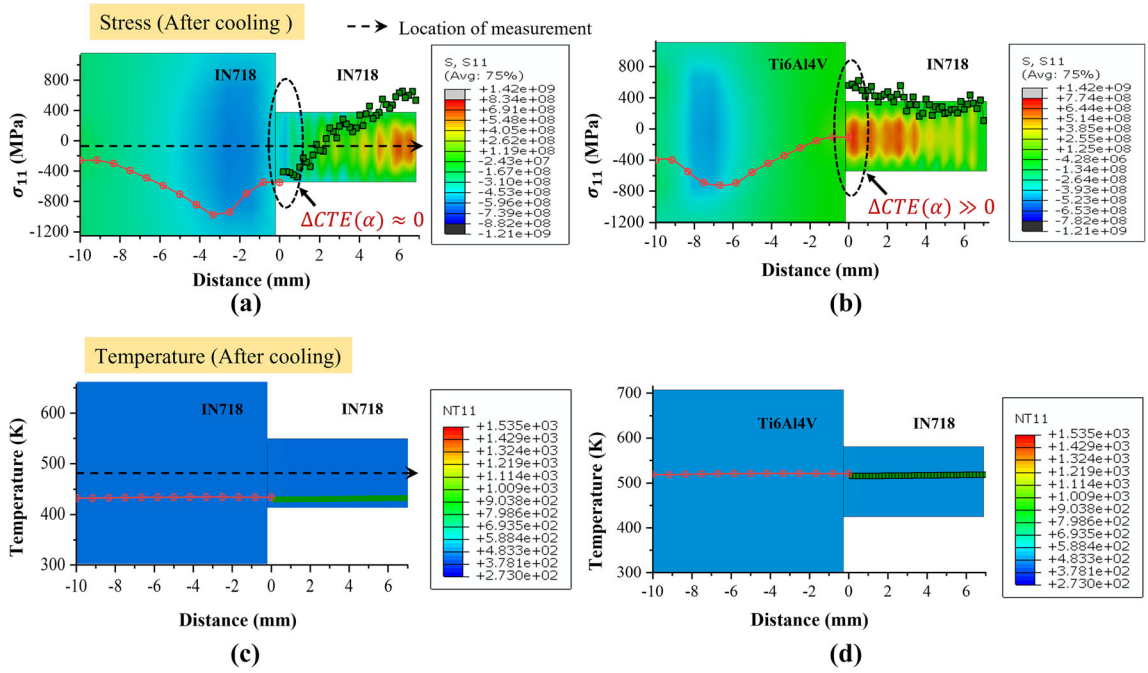

Fig. 13—Residual stress component, σ_{11} in (*a*) 10IN/IN and (*b*) 10Ti/IN and corresponding temperature distribution after cooling (*c*) 10IN/IN and (*d*) 10Ti/IN.

cooling down 10IN/IN and 10IN/Ti. The temperature was reduced to 434 K and maximum tensile stresses of ~ 655 MPa were attained in at and near the top layer in the 10IN/IN(IN718 substrate). This could be due to the fact that there was no reheating of the top layer to partially alleviate the tensile residual stress. As discussed earlier, the stresses were tensile in nature in the 1st and 2nd layers after the deposition of the 2nd layer. However, the subsequent depositions and diffusion of accumulated heat from successive layers to the underlying layers near the substrate relieved the tensile residual stresses and transformed to compressive stresses of ~550 MPa. Since both the substrate and deposited material are IN718, ΔCTE has no contribution to the residual stress generation in 10IN/IN. This behaviour of residual stress pattern was also revealed in previous studies.[1,28,40] Zhou et al, reported tensile longitudinal stress near the depositing layers due to the contraction of depositing material at cooling stage, whereas it was found to be compressive at location far away from depositing layers in order to balance the stress in the whole system.[1,9,40]

The overall temperature of 10IN/Ti reached 520 K after the same cooling time of 100 s. The location of the maximum tensile residual stress of ~ 621 MPa was reversed from the top layer to layers close to the substrate. In this context, it is noteworthy that the coefficient of thermal expansion (CTE) of IN718 (13×10^{-6} K^{-1}) is ~ 1.5 times higher than Ti6Al4V alloy (8.7×10^{-6} K^{-1}). Under these circumstances, the IN718 deposited close to the substrate contracted substantially more than Ti6Al4V substrate during the cooling cycle and generated relatively high tensile residual strain/stress close to the IN718/Ti6Al4V interface. However, the temperature gradient was comparatively less effective and generated lower tensile residual stresses of ~ 410 MPa near the top layer. As stated earlier, the Ti6Al4V substrate decreases the thermal gradient and can alter the stress distribution pattern. However, the localization of tensile stresses at interface can enhance the propensity of delamination, if the yield stress is exceeded. Upon exceeding the yield strength value, it would cause a deviation from the intended shape of the build and detrimentally affect the fracture toughness and fatigue behaviour and, accelerates the crack growth mechanism as well.[40]

V. CONCLUSIONS

This study provides new insights into thermal response, solidification behaviour and mechanism of residual stress formation in laser-additively manufactured single- (IN718-IN718) and multi-material (IN718-Ti6Al4V) systems. These systems were simulated as laser-based direct energy deposition process by admixing a sequential coupled thermo-mechanical model and validated with experimental measurements from literature. The following conclusions were made based on the present investigation:

- The developed model minimized the complexity of considering convective heat loss due to fluid flow involved during the metal melting by including linearly enhanced thermal conductivity, and qualitative agreement was achieved between thermal as well as mechanical models and experimental measurements.

- The heat sink effect offered by dissimilar substrates was effective only up to the deposition of 4 to 5 layers. Both 10IN/IN and 10IN/Ti exhibited similar thermal characteristics (melt pool size, solidification velocity) for higher layers.
- The difference in highest temperatures of 1799 K in the Ti6Al4V substrate due to low thermal conductivity, as compared to 1599 K in the IN718 substrate was sufficient to alter the solidification behaviour as well as the residual stress distribution in the deposited metal.
- The accumulation of high thermal energy in the Ti6Al4V substrate lead to low solidification velocity (2.02 mm/s) and low cooling rate (3050 K/s) in the 1st layer relative to IN718 substrate system. In addition, this also formed a relatively large melt pool (0.95 mm) and high PDAS ~ 10.8 μm due to ample grain coarsening time in 10IN/Ti.
- The reversal of maximum tensile residual stress (σ_{11} ~ 621 to 655 MPa) location from top 10th layer to the bottom 1st layer occurred due to a significant ΔCTE accomplished by changing the substrate from IN718 to Ti6Al4V. Hence, ΔCTE was determined as the important factor for the residual stress evolution in the multi-material system, whereas the thermal gradient governed the residual stresses in a single-material system.
- The Ti6Al4V substrate decreased the thermal gradient and also transformed the stress distribution pattern. However, the localization of tensile stresses at the interface enhances the possibility of warping and delamination on exceeding the yield stress.

ACKNOWLEDGMENTS

The authors gratefully acknowledge the Department of Metallurgical Engineering and Materials Science of Indian Institute of Technology Bombay for providing the computational facility along with licensed ABAQUS® commercial software.

CONFLICT OF INTEREST

On behalf ofall authors, the corresponding author states that there are no conflicts of interest.

REFERENCES

1. L.Y. Zhou, J. Fu, and Y. He: *Adv. Funct. Mater.*, 2020, vol. 30, pp. 1–38.
2. A. Le Duigou, M. Castro, R. Bevan, and N. Martin: *Mater. Des.*, 2016, vol. 96, pp. 106–14.
3. Y.W.D. Tay, M.Y. Li, and M.J. Tan: *J. Mater. Process. Technol.*, 2019, vol. 271, pp. 261–70.
4. A. Bandyopadhyay and B. Heer: *Mater. Sci. Eng. R*, 2018, vol. 129, pp. 1–6.
5. E. Mirkoohi, J.R. Dobbs, and S.Y. Liang: *Int. J. Adv. Manuf. Technol.*, 2020, vol. 106, pp. 4105–21.
6. E. Mirkoohi, D.E. Sievers, H. Garmestani, and S.Y. Liang: *CIRP J. Manuf. Sci. Technol.*, 2020, vol. 28, pp. 52–67.
7. E. Mirkoohi, J.R. Dobbs, and S.Y. Liang: *J. Manuf. Process.*, 2020, vol. 58, pp. 41–54.
8. Z.C. Fang, Z.L. Wu, C.G. Huang, and C.W. Wu: *Opt. Laser Technol.*, 2020, vol. 129, p. 106283.
9. Q. Wu, T. Mukherjee, C. Liu, J. Lu, and T. DebRoy: *Addit. Manuf.*, 2019, vol. 29, p. 100808.
10. A.M. Kamara, W. Wang, S. Marimuthu, and L. Li: *Proc. Inst. Mech. Eng. Part B*, 2011, vol. 225, pp. 87–99.
11. Q. Jia and D. Gu: *J. Alloys Compd.*, 2014, vol. 585, pp. 713–21.
12. S.Y. Gaol, Y.Z. Zhang, L.K. Shi, and B.L. Du: 2007, pp. 171–80.
13. S. Maietta, A. Gloria, G. Improta, M. Richetta, R. De Santis, and M. Martorelli: *J. Healthc. Eng.*, 2019, https://doi.org/10.1155/2019/3212594.
14. C. Qiu, N.J.E. Adkins, and M.M. Attallah: *Mater. Sci. Eng. A*, 2013, vol. 578, pp. 230–39.
15. L.Y. Chen, J.C. Huang, C.H. Lin, C.T. Pan, S.Y. Chen, T.L. Yang, D.Y. Lin, H.K. Lin, and J.S.C. Jang: *Mater. Sci. Eng. A*, 2017, vol. 682, pp. 389–95.
16. P. Kyvelou, H. Slack, D. Daskalaki Mountanou, M.A. Wadee, T. Ben Britton, C. Buchanan, and L. Gardner: *Mater. Des.*, 2020, vol. 192, p. 108675.
17. V. Laghi, L. Tonelli, M. Palermo, M. Bruggi, R. Sola, L. Ceschini, and T. Trombetti: *Addit. Manuf.*, 2021, vol. 42, p. 101999.
18. M. Ghaffari, A. Vahedi Nemani, M. Rafieazad, and A. Nasiri: *Jom*, 2019, vol. 71, pp. 4215–24.
19. X. Wang, X. Gong, and K. Chou: *Proc. Inst. Mech. Eng. Part B*, 2017, vol. 231, pp. 1890–1903.
20. G.P. Dinda, A.K. Dasgupta, and J. Mazumder: *Mater. Sci. Eng. A*, 2009, vol. 509, pp. 98–104.
21. N.A. Kistler, A.R. Nassar, E.W. Reutzel, D.J. Corbin, and A.M. Beese: *J. Laser Appl.*, 2017, vol. 29, p. 022005.
22. J.S.K.E.W.R. Cory, D. Jamieson, Marissa C. Brennan, Todd J. Spurgeon, Stephen W. Brown: *J. Laser Appl.* https://doi.org/10.2351/7.0000534.
23. M. Bambach, I. Sizova, F. Kies, and C. Haase: *Addit. Manuf.*, 2021, vol. 47, p. 102269.
24. Z. Liu, B. He, T. Lyu, and Y. Zou: *Jom*, 2021, vol. 73, pp. 1804–08.
25. Y. Lu, S. Wu, Y. Gan, T. Huang, C. Yang, L. Junjie, and J. Lin: *Opt. Laser Technol.*, 2015, vol. 75, pp. 197–206.
26. P. Rangaswamy, M.L. Griffith, M.B. Prime, T.M. Holden, R.B. Rogge, J.M. Edwards, and R.J. Sebring: *Mater. Sci. Eng. A*, 2005, vol. 399, pp. 72–83.
27. L. Wang, S.D. Felicelli, and P. Pratt: *Mater. Sci. Eng. A*, 2008, vol. 496, pp. 234–41.
28. R.J. Moat, A.J. Pinkerton, L. Li, P.J. Withers, and M. Preuss: *Mater. Sci. Eng. A*, 2011, vol. 528, pp. 2288–98.
29. N. Nadammal, S. Cabeza, T. Mishurova, T. Thiede, A. Kromm, C. Seyfert, L. Farahbod, C. Haberland, J.A. Schneider, P.D. Portella, and G. Bruno: *Mater. Des.*, 2017, vol. 134, pp. 139–50.
30. J. Hönnige, C.E. Seow, S. Ganguly, X. Xu, S. Cabeza, H. Coules, and S. Williams: *Mater. Sci. Eng. A*, 2020, https://doi.org/10.1016/j.msea.2020.140368.
31. K. Kempen, L. Thijs, B. Vrancken, S. Buls, J. Van Humbeeck, and J.P. Kruth: *24th Int. SFF Symp. - An Addit. Manuf. Conf. SFF 2013*, 2013, pp. 131–39.
32. P.J. Withers and H.K.D.H. Bhadeshia: *Mater. Sci. Technol.*, 2001, vol. 17, pp. 355–65.
33. A.H. Nickel, D.M. Barnett, and F.B. Prinz: *Mater. Sci. Eng. A*, 2001, vol. 317, pp. 59–64.
34. E.R. Denlinger, J.C. Heigel, P. Michaleris, and T.A. Palmer: *J. Mater. Process. Technol.*, 2015, vol. 215, pp. 123–31.
35. B.A. Szost, S. Terzi, F. Martina, D. Boisselier, A. Prytuliak, T. Pirling, M. Hofmann, and D.J. Jarvis: *Mater. Des.*, 2016, vol. 89, pp. 559–67.
36. C. Li, Z.Y. Liu, X.Y. Fang, and Y.B. Guo: *Procedia CIRP*, 2018, vol. 71, pp. 348–53.
37. A.S. Wu, D.W. Brown, M. Kumar, G.F. Gallegos, and W.E. King: *Metall. Mater. Trans. A*, 2014, vol. 45A, pp. 6260–70.
38. M.F. Zaeh and G. Branner: *Prod. Eng.*, 2010, vol. 4, pp. 35–45.
39. J.P. Kruth, J. Deckers, E. Yasa, and R. Wauthlé: *Proc. Inst. Mech. Eng. Part B*, 2012, vol. 226, pp. 980–91.

40. T. Mukherjee, W. Zhang, and T. DebRoy: *Comput. Mater. Sci.*, 2017, vol. 126, pp. 360–72.
41. M. McMillan, M. Leary, and M. Brandt: *Mater. Des.*, 2017, vol. 132, pp. 226–43.
42. J. Wang, Y. Wang, and J. Shi: *Int. J. Precis. Eng. Manuf.*, 2021, vol. 8, pp. 1181–96.
43. C. Carmignani, R. Mares, and G. Toselli: *Comput. Methods Appl. Mech. Eng.*, 1999, vol. 179, pp. 197–214.
44. N. Keller and V. Ploshikhin: *25th Annu. Int. Solid Free. Fabr. Symp. &#65533; An Addit. Manuf. Conf. SFF 2014*, 2014, pp. 1229–37.
45. P. Mercelis and J.P. Kruth: *Rapid Prototyp. J.*, 2006, vol. 12, pp. 254–65.
46. T. Simson, A. Emmel, A. Dwars, and J. Böhm: *Addit. Manuf.*, 2017, vol. 17, pp. 183–89.
47. K. Shah, I.U. Haq, S.A. Shah, F.U. Khan, M.T. Khan, and S. Khan: *Sci. World J.*, 2014, https://doi.org/10.1155/2014/841549.
48. F. Lia, J. Park, J. Tressler, and R. Martukanitz: *Addit. Manuf.*, 2017, vol. 18, pp. 31–39.
49. B. Kumar and S. Bag: *Opt. Lasers Eng.*, 2019, vol. 122, pp. 209–24.
50. B. Taljat, B. Radhakrishnan, and T. Zacharia: *Mater. Sci. Eng. A*, 1998, vol. 246, pp. 45–54.
51. A.S. Agazhanov, D.A. Samoshkin, and Y.M. Kozlovskii: *J. Phys. Conf. Ser.*, 2019, https://doi.org/10.1088/1742-6596/1382/1/012175.
52. B. Kumar, S. Bag, S. Mahadevan, C.P. Paul, C.R. Das, and K.S. Bindra: *CIRP J. Manuf. Sci. Technol.*, 2021, vol. 33, pp. 158–75.
53. J.S. Lee, J.H. Gu, H.M. Jung, E.H. Kim, Y.G. Jung, and J.H. Lee: *Mater. Today Proc.*, 2014, vol. 1, pp. 3–10.
54. M. Gäumann, C. Bezençon, P. Canalis, and W. Kurz: *Acta Mater.*, 2001, vol. 49, pp. 1051–62.
55. Y. Lee, M. Nordin, S.S. Babu, and D.F. Farson: *Metall. Mater. Trans. B*, 2014, vol. 45B, pp. 1520–29.
56. S. Bontha, N.W. Klingbeil, P.A. Kobryn, and H.L. Fraser: *Mater. Sci. Eng. A*, 2009, vol. 513–514, pp. 311–18.
57. W. Kurz and D.J. Fisher: *Acta Metall.*, 1981, vol. 29, pp. 11–20.
58. R. Trivedi: *J. Cryst. Growth*, 1980, vol. 49, pp. 219–32.
59. W. Wang, P.D. Lee, and M. McLean: *Acta Mater.*, 2003, vol. 51, pp. 2971–87.
60. K. Yuan, W. Guo, P. Li, Y. Zhang, X. Li, and X. Lin: *Mech. Mater.*, 2019, vol. 135, pp. 13–25.
61. G. Chen, C. Ren, X. Qin, and J. Li: *Mater. Des.*, 2015, vol. 83, pp. 598–610.
62. T. Singh and V.K. Gupta: *Mech. Adv. Mater. Struct.*, 2014, vol. 21, pp. 384–92.
63. X. Song, S. Feih, W. Zhai, C.N. Sun, F. Li, R. Maiti, J. Wei, Y. Yang, V. Oancea, L. Romano Brandt, and A.M. Korsunsky: *Mater. Des.*, 2020, vol. 193, p. 108779.
64. V. Manvatkar, A. De, and T. Debroy: *J. Appl. Phys.*, 2007, https://doi.org/10.1063/1.4896751.
65. V. Manvatkar, A. De, and T. DebRoy: *Mater. Sci. Technol. (United Kingdom)*, 2015, vol. 31, pp. 924–30.
66. D. Grange, J.D. Bartout, B. Macquaire, and C. Colin: *Materialia*, DOI:https://doi.org/10.1016/j.mtla.2020.100686.
67. H. Qi, J. Mazumder, and H. Ki: *J. Appl. Phys.*, DOI:https://doi.org/10.1063/1.2209807.
68. X. He and J. Mazumder: *J. Appl. Phys.*, 2007, https://doi.org/10.1063/1.2710780.
69. C. Guévenoux, S. Hallais, A. Charles, E. Charkaluk, and A. Constantinescu: *Opt. Laser Technol.*, 2020, vol. 128, p. 106218.
70. G. Langelandsvik, O.M. Akselsen, T. Furu, and H.J. Roven: *Materials (Basel)*, 2021, vol. 14, pp. 1–26.
71. B. Bellón, A. Boukellal, T. Isensee, O.M. Wellborn, K.P. Trumble, M.J.M. Krane, M.S. Titus, D. Tourret, and J. LLorca: *Acta Mater.*, 2021, https://doi.org/10.1016/j.actamat.2021.116686.
72. X. Zhang, B. Mao, L. Mushongera, J. Kundin, and Y. Liao: *Mater. Des.*, 2021, vol. 201, p. 109501.
73. D. Guo, K. Yan, M.D. Callaghan, D. Daisenberger, M. Chatterton, J. Chen, A. Wisbey, and W. Mirihanage: *Mater. Des.*, 2021, vol. 207, p. 109782.